30th Congress of the International Council
of the Aeronautical Sciences
DCC, Daejeon, Korea ; September 25-30, 2016

EFFECT OF ELASTIC DEFORMATION ON FLIGHT DYNAMICS OF PROJECTILES WITH LARGE SLENDERNESS RATIO

HUA RuHao, YE ZhengYin, YANG Lei
School of Aeronautics, Northwestern Polytechnical University, Xi’an, 710072, China

Keywords: *elastic deformation; flight dynamics; six degree of freedom motion; large slenderness ratio*

Abstract

The elastic deformation of the newly projectiles with large slenderness ratio cannot be ignored with the increasing of flight speed and high maneuverability. Reynolds-averaged Navier-Stokes Equations are solved through CFD technique in this paper. Based on the frame of unstructured mesh, techniques of rigid-motion mesh and inverse-distance-weighted morphing mesh are adopted to treat the rigid motion of six degree of freedom(SDOF) caused by flight dynamics and flexible structure deformation caused by aeroelasticity respectively. Moreover, the six-degree freedom dynamic equations are solved with static aeroelastic equations with the mode-summation method. Numerical results of free flight case and static aeroelasticity case calculated using the in-house code both agree well with the experimental data respectively, which shows the validation of the numerical method. An air-to-air projectile model of X-X configuration is constructed to research the effect of elastic deformation on the trajectory of the projectiles with large slenderness ratio. Comparison results of flexible and rigid models show that the longitudinal and course trajectory of centroid is affected by the elastic deformation, and the oscillatory cycle of the orientation angle increases. Furthermore, the trajectories of rigid models with various centroid locations are computed, illustrating that the elastic deformation could move the aerodynamic center forward and weaken the margin of the stability.

1 Introduction

Large thrust-to-weight and length-to-diameter (slenderness) ratio of projectiles are needed to launch heavier payloads, increase range, and reduce aerodynamic drag. The aforementioned requirements lead to a highly flexible launch vehicle, for which dynamic response and vibration characteristics are of vital importance. As the slenderness ratio increases, the structure becomes more flexible, and the natural frequencies of transverse vibration decrease. Accordingly, it is of high importance to regard behaviors of the objects as flexible models to ensure the flight safety and accurate arrival of the munitions at the target. The early missiles and projectiles with smaller ratio of slenderness and denser structures can be reasonably regarded as rigid models for dynamic analysis, while the elastic deformation of the newly practical missile due to aerodynamic loads cannot be ignored with the increasing of flight speed and high maneuverability, which might be beyond the range of common tolerance introduced in manufacturing [1-4]. Since the structural rigidity and natural frequencies of free vibration is lower, it is easier for the air-to-air missiles and rocket missiles with larger slenderness ratio to deform during the process of maneuvering rapidly or separating from aircrafts, which not only has adverse effect on the trajectory and firing accuracy, but also causes uncertain threat to the carrier. Moreover, fairings of large carrier rockets are more prone to aeroelastic problems such as breathing deformation due to thin-wall structures [5], which makes it more difficult to predict the trajectory of the separated components suffering from serious aerodynamic interference.

Since flight dynamics of flexible vehicles is involved in significant mutual interaction among aerodynamics, flight mechanics, elastic forces and control systems [6,7], it cannot be calculated easily and accurately by engineering methods. Previous studies have handled with the problem with simplified models which have lots of assumptions and limitations. Reis addressed the problem of aeroelastic bending of spinning sounding rockets using a simple two-rigid-body model and pointed out that traverse bending of the free-flight rocket could lead to obvious lateral angular velocity [6]. Womack discussed the use of a more complex model based on the use of normal modes to model the flexibility of such rockets [7]. Based on the Euler-Bernoulli beam model and Hamilton's principle, Wang undertook trajectory simulation of a rocket and found that the range of the rocket could be increased while the flight level became lower compared to the results of rigid-body models [8].

Although a great deal of work has been expanded to test the effects of flexibility on the stability of projectiles and launch vehicles, simplified models are always adopted. The aerodynamic forces which dominate the trajectory are normally predicted with lifting-line method or perturbation method. Additionally, more researches related to the coupling of elastic deformation and flight dynamic characteristics focus on the flight vehicle itself, while the investigation about mechanics of the effect of aeroelasticity is very limited.

Since the accuracy of the engineering method is limited and will lead to more cumulative errors, it is necessary to develop more exact methods to predict the characteristics of the flight dynamics of the flexible projectiles. Schütte at DLR simulated the unsteady aerodynamics of a free-flying aeroelastic combat aircraft by use of coupled aerodynamic, flight mechanics, and aeroelastic computations with the flow-solver TAU [9]. The CREATE-AV Project established by the DoD (the United States Department of Defense) is tasked to develop, deploy and support a set of multidisciplinary, physics-based simulation software products for the engineering workforces supporting air vehicle acquisition programs, and the project could handle the problems related to flexible aircraft with SDOF motion and moving control surfaces [10,11]. Based on the frame of unstructured hybrid mesh, the method combining rigid-motion mesh technique with mesh deformation is applied to the problem coupling the rigid body motion and structural elasticity. Unsteady Navier-Stokes (NS) equations are solved to obtain the aerodynamic forces and moments at different time. Flight dynamic equation based on the SDOF motion and static aeroelastic equation based on the modal approach are solved to investigate the interaction of the flight dynamics and elastic deformation.

2 Overview of the Framework for flight dynamics coupled with Aeroelasticity

The frame of the solving methodology present in this paper is shown in Fig.1, which mainly consists of three modules including grid-treating module, CFD solver module and fluid-solid interaction module. The grid-treating module is capable of adapting elastic deformation of the meshes caused by aeroelasticity and adjusting the new computational domains according to the large rigid displacement caused by SDOF motion. The flow solver module is used to obtain the numerical results of the governing fluid equations at each time step. With the solution in CFD solver module, the aerodynamic forces and moments on the store are computed by integrating the pressure over the surface. Meanwhile, the generalized forces needed for the modal approach could also be obtained [12,13]. The rigid motion and the elastic deformation of the flight vehicle can be computed by the SDOF trajectory codes and the aeroelastic codes in the fluid-solid interaction module respectively.

The method is a loosely coupled system, and the effect of the aeroelasticity on the flight dynamics is embodied in the new location of the mesh nodes. The combined mesh node movement is the summation of the rigid displacement and the elastic deformation from the fluid-solid interaction module. Correspondingly, the flow field is composed of the effect of both flight dynamics and aeroelasticity. Various components of this framework are described next.

2.1 Dynamic Mesh Technique

With the rapid progress in the field of computer science and technology, more detailed and complicated configurations can be treated. It is widely acknowledged that unstructured meshes are more convenient and flexible than structured grids to handle complex models. Here hybrid unstructured meshes are selected for the simulation of the flow fields in this paper. The rigid-motion mesh technique is adopted to treat the large rigid-body displacement due to the motion of SDOF, while the flexible structure deformation caused by aeroelasticity is dealt with by an inverse-distance weighted morphing mesh method.

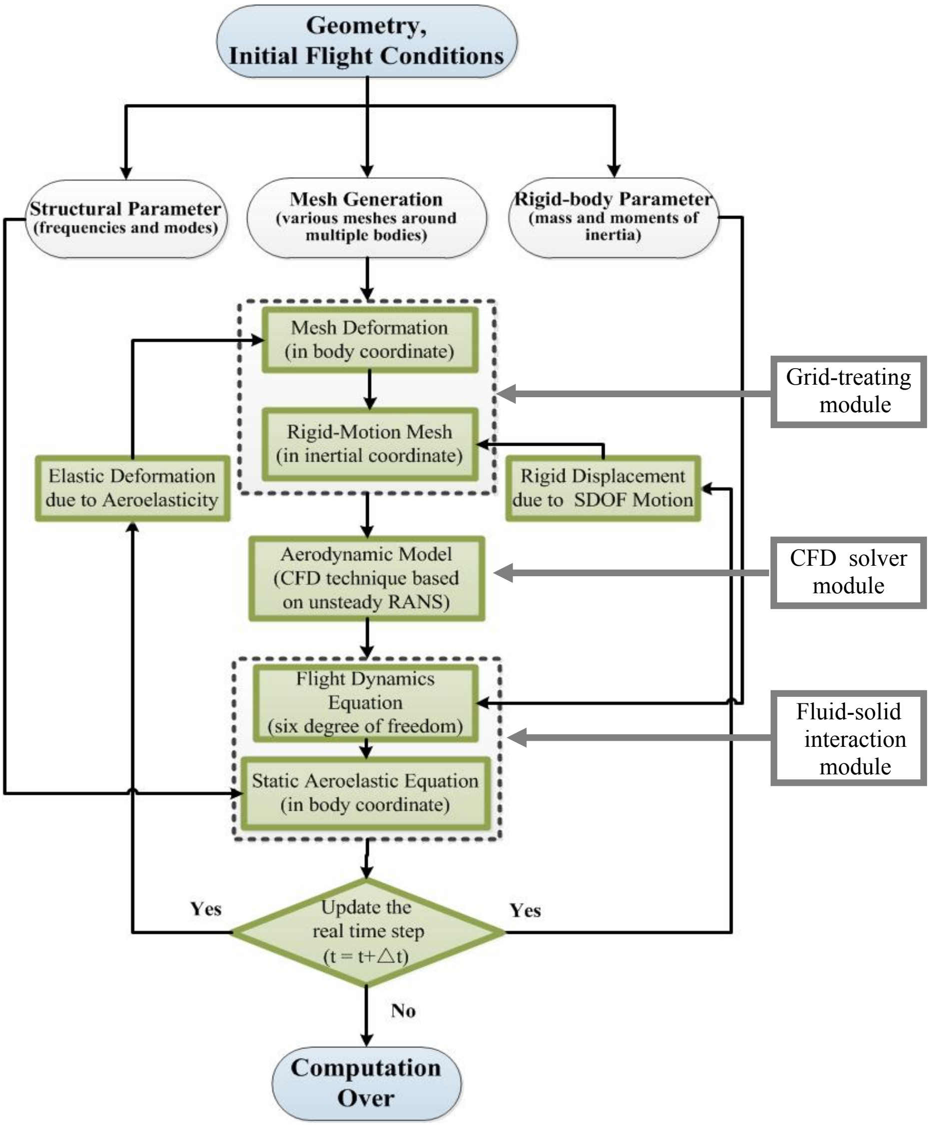

Fig. 1. Flow Chart of the Solving Methodology

2.1.1 Rigid-motion Mesh technique

The basic idea of the rigid-motion mesh technique is to update the location of all nodes of the computational mesh according to the translational displacement of the centroid and the rotation around the centroid. Here, the displacement of the centroid and the orientation angles could be obtained through solving the flight dynamic equation in each time step. The distinct advantage of the rigid-motion mesh technique is that the computational mesh could be obtained directly without being reconstructed during the numerical simulation process, which not only reduces the computational cost of each time step dramatically, but also keeps the topological relationship the quality of the computational mesh.

Here define $\vec{r}_0$ is the coordinate of the node of the computational mesh in inertial system at the initial moment, then the new location $\vec{r}$ of the corresponding node during the simulation process could be expressed as

$$\vec{r} = \vec{r}_0 + \Delta\overrightarrow{r_{cg}} + \Delta\overrightarrow{r_{rot}} \tag{1}$$

Where $\Delta\overline{r_{cg}}$ is the displacement of the centroid of the moving body, $\Delta\overline{r_{rot}}$ is the displacement due to the rotation around the centroid, which could be obtained through Eq.(2)

$$\Delta\overrightarrow{\boldsymbol{r}_{rot}} = \boldsymbol{T} \bullet (\vec{\boldsymbol{r}}_0 - \vec{\boldsymbol{r}}_{0,\boldsymbol{cg}}) \tag{2}$$

The transformation matrix in (2) could be expressed as

$$\mathrm{T}_{B-I} = \mathrm{T}_{B-I}^{\phi}\mathrm{T}_{B-I}^{\theta}\mathrm{T}_{B-I}^{\psi} =$$

$$\begin{bmatrix} \cos\theta\cos\psi & -\cos\theta\sin\psi & \sin\theta \\ \cos\phi\sin\psi + \sin\phi\sin\theta\cos\psi & \cos\phi\cos\psi - \sin\phi\sin\theta\sin\psi & -\sin\phi\cos\theta \\ \sin\phi\sin\psi - \cos\phi\sin\theta\cos\psi & \sin\phi\cos\psi + \cos\phi\sin\theta\sin\psi & \cos\phi\cos\theta \end{bmatrix} \tag{3}$$

2.1.2 Mesh Deformation Method

Taking flexible effect into consideration during the simulation of the free flight process, elastic deformation caused by external forces exists except for the dominant displacement due to rigid-body motion in each movable zone. Each nodal position on the boundaries is determined with the summation of the elastic deformation through solving the aeroelastic equation and the position of the original rigid model.

In this paper an inverse distance-weighted (IDW) method is employed with the establishment of a special weighting function to distribute the displacements of surfaces [12]. The interpolation function is expressed as:

$$w(\mathbf{x}_i) = \frac{\sum\limits_{ib\in\Xi(B)} \left[\left(\|\Delta\mathbf{x}_{ib}\| \right)^a \cdot w(\mathbf{x}_{ib}) \right]}{\sum\limits_{ib\in\Xi(B)} \left(\|\Delta\mathbf{x}_{ib}\| \right)^a} \tag{4}$$

Where $\Xi(B)$ represents the boundary point set and $w(\mathbf{x}_i)$ is the displacements of the node I and $\Delta\mathbf{x}_{ib} = \mathbf{x}_{ib} - \mathbf{x}_i$.

2.2 Governing Equations of Fluid Flow and Numerical Method

The conservation form of governing equations for unsteady, three dimensional, compressible and viscous flow can be written in an integral form as follows

$$\frac{\partial}{\partial t}\iiint\limits_{\Omega} \mathbf{Q}\,\mathrm{d}V + \iint\limits_{\partial\Omega} \mathbf{F}(\mathbf{Q}, \mathbf{V}_{grid}) \cdot \mathbf{n}\,\mathrm{d}S = \iint\limits_{\partial\Omega} \mathbf{F}^V(\mathbf{Q}) \cdot \mathbf{n}\,\mathrm{d}S \tag{5}$$

Where $\mathbf{Q} = [\rho, \rho u, \rho v, \rho w, e]^T$ is the vector of conservative variables; ρ is the density; u, v and w are the velocity components in the x, y and z directions respectively; e is the total energy. $\mathbf{F}(\mathbf{Q}, \mathbf{V}_{grid})$ and $\mathbf{F}^V(\mathbf{Q})$ are the inviscid flux vector and the viscous flux vector respectively; $\mathbf{V}_{\mathrm{grid}}$ is the velocity vector of a control volume due to SDOF motion and elastic deformation. Ω represents a control volume with the boundaries expressed as $\partial\Omega$ and $\mathbf{n}$ is the normal vector of the boundary face of a control volume.

A cell-centered finite volume method is employed based on unstructured hybrid meshes composed of hexahedrons, prisms, tetrahedrons and pyramids. More details are given in Ref [13]. Moreover, the spatial discretization AUSM+ scheme is used with an implicit LU-SGS scheme for the temporal integration.

2.3 Solution of Flight Dynamics Equations and Aeroelastic Equations

As illustrated in Fig.1, the loosely coupled method is used for the complicated aerial separation. When finishing the solution of a real time step of the unsteady flow, we obtain the aerodynamic parameters all over the flow field. With the aerodynamics forces and moments through the integration of the pressure over the wall surface, the movement of the objects can be calculated by numerically integrating the flight dynamic equation of SDOF, while the structural deformation can be obtained by means of solving the aeroelastic equation. The nodal locations of the new meshes could be regarded as the summation of the separated object movement caused by SDOF motion and the elastic deformation due to aeroelastic effect.

2.3.1 Rigid Body Motion Equations of SDOF

The rigid body motion is disassembled into the centroid translation and rotational motion around the centroid. Translational motion can be easily calculated by Newton's Law as follows

$$m\ddot{\mathbf{x}}_{\mathrm{cg}}^{\mathrm{I}} = \mathbf{F}_{\mathrm{a}}^{\mathrm{I}} + \mathbf{F}_{\mathrm{e}}^{\mathrm{I}} + \mathbf{F}_{\mathrm{g}}^{\mathrm{I}} \tag{6}$$

Where m is the mass of the object, $\ddot{\mathbf{x}}_{\mathrm{cg}}^{\mathrm{I}}$ is the acceleration vector of the centroid, and $\mathbf{F}_{\mathrm{a}}^{\mathrm{I}}$, $\mathbf{F}_{\mathrm{e}}^{\mathrm{I}}$, $\mathbf{F}_{\mathrm{g}}^{\mathrm{I}}$ are the aerodynamic force, external forces(such as ejection forces) and the forces of gravity respectively. Moreover, the superscript I represents the inertial coordinates.

According to the theorem of moment of momentum about the centroid, the dynamic equation of rigid body rotation could be readily expressed in the body coordinates as follows

$$\frac{d\mathbf{H}}{dt} = \mathbf{M} \tag{7}$$

Where **H** is the vector of the moment of momentum around the rigid centroid and **M** is the resultant moment vector caused by aerodynamic forces and the external forces.

After introducing Euler motion relationship, the system of Eq. (8) for flight dynamics regardless of time derivatives of inertia matrix could be expressed as

$$\begin{cases} m\ddot{\mathbf{x}}_{\mathrm{cg}}^{\mathrm{I}} = \sum \mathbf{F} \\ \dot{\boldsymbol{\varphi}} = \mathbf{T}\boldsymbol{\omega} \\ \dot{\boldsymbol{\omega}} = -\mathbf{I}^{-1}\boldsymbol{\omega}^{ss}\mathbf{I}\boldsymbol{\omega} + \mathbf{I}^{-1}\mathbf{M} \end{cases} \tag{8}$$

Where $\boldsymbol{\omega} = [\omega_x, \omega_y, \omega_z]^T$ and $\boldsymbol{\varphi} = (\varphi \quad \theta \quad \psi)^T$ are the angular velocity in the body coordinate and the inertial system respectively, **I** is the inertia matrix. $\boldsymbol{\omega}^{ss}$ is the skew symmetric matrix of $\boldsymbol{\omega}$, and it has the expression as follows

$$\boldsymbol{\omega}^{ss} = \begin{bmatrix} 0 & -\omega_z & \omega_y \\ \omega_z & 0 & -\omega_x \\ -\omega_y & \omega_x & 0 \end{bmatrix} \tag{9}$$

T is the trans-formation matrix which could be expressed as:

$$\mathbf{T} = \begin{bmatrix} 1 & \sin\varphi\tan\theta & \cos\varphi\tan\theta \\ 0 & \cos\varphi & -\sin\varphi \\ 0 & \sin\varphi/\cos\theta & \cos\varphi/\cos\theta \end{bmatrix} \tag{10}$$

A hybrid linear multi-step scheme is applied to solve Eq. (8), the one-order ordinary differential equation. Two-order semi-implicit linear multi-step scheme (SILMS) is employed for the time marching of flight dynamic equations [14].

2.3.2 Static Aeroelastic Equation Based on the Mode-Summation Method

Structural deformation needs to be obtained by means of computational structural dynamics (CSD) technique. Nevertheless, while the elastic deformation is limited compare to the characteristic length of the rigid model and the structure is of good linear characteristics, the structural elasticity could be introduced from a modal decomposition of the discrete finite element model. Thus it leads to a linearly approximated elastic model based on a reduced number of modal degrees of freedom, which could be named as the modal approach [15, 16]. This method has been used as one of the most practical approach during the analysis of structural dynamics of linear systems for its higher efficiency compared to the technique of the finite element method (FEM) which needs large amounts of time for iterations.

Since the scale of the elastic deformation in this paper is much smaller than the characteristic length of the rigid projectile model. Consequently the modal approach is adopted in this paper to solve the structural deformation.

While N modes are used to describe the structural deformation in the modal approach, the deformation of the wall of the elastic model is subsequently determined by

$$\mathbf{w}(t) = \sum_{i=1}^{N} \boldsymbol{\Phi}_i q_i(t) \tag{11}$$

Where w is the elastic displacement of structural deformations, $\boldsymbol{\Phi}_i$ is the ith-order mode which could be obtained by FEM or mode tests, q_i is the generalized coordinate of the ith order mode.

The final aeroelastic equations based on the modal approach could be expressed as:

$$\mathbf{M}\ddot{\mathbf{q}} + \mathbf{C}\dot{\mathbf{q}} + \mathbf{K}\mathbf{q} = \mathbf{Q} \tag{12}$$

Where **M**, **K** and **C** are the generalized mass matrix, the generalized stiffness matrix and generalized structural damping matrix respectively. And the generalized force **Q** can be calculated via $\mathbf{Q}_i = \iint P\boldsymbol{\Phi}_i \cdot \mathrm{d}\mathbf{S},\ i \in [1, \ \cdots, \ N]$, where P is the pressure distribution on the bodies and **S** represents the normal vector of a surface.

Noticeably, Eq. (12) is constructed in the body coordinates, which ensures that the structural modes keep constant during the flight trajectory. Furthermore, when static aeroelasticity is dealt with, all terms of $\mathbf{M}\ddot{\mathbf{q}}$ and $\mathbf{C}\dot{\mathbf{q}}$ should be set to 0. Hence, we obtain an N-dimensional linear equation expressed via Eq. (13).

$$\mathbf{K}\mathbf{q} = \mathbf{Q} \tag{13}$$

Combining Eq. (8) and (13), we can obtain the system of Eq. (14) which is needed in the fluid-solid interaction module.

$$\begin{cases} m\ddot{\mathbf{x}}_{\mathrm{cg}}^{\mathrm{I}} = \sum \mathbf{F} \\ \dot{\boldsymbol{\varphi}} = \mathbf{T}\boldsymbol{\omega} \\ \dot{\boldsymbol{\omega}} = -\mathbf{I}^{-1}\boldsymbol{\omega}^{ss}\mathbf{I}\boldsymbol{\omega} + \mathbf{I}^{-1}\mathbf{M} \\ \mathbf{q} = \mathbf{K}^{-1}\mathbf{Q} \end{cases} \tag{14}$$

During time marching for the simulation of the aerial separation, the rigid body motion and the elastic body motion in Eq. (14) are solved after the computation of the unsteady flow field. The interference between the elastic deformation and the displacement of SDOF motion is coupled through their contribution to the new locations of the mesh nodes.

3 Computational Cases and Analysis

3.1 Verification Case of Spinning Projectile

An ARL spinning projectile configuration is selected as the computational model, since it has detailed experimental data [17-18]. The geometric parameters can be seen in Fig. 2 where the unit is millimeter. The projectile is constituted by ogive nose, cylinder and four fins. The ogive nose is 98.6 *mm* long and the afterbody of the cylinder has a boat tail of 22.4 *mm* and 2.5 *deg*. The fins have a thickness of 1.02 mm, a sweep angle of approximately 30 *deg*, a 25 *mm* span, a 22.3 *mm* root chord and a 10.3 *mm* tip chord. The fins have the same constant thickness everywhere, including the leading and trailing edge. Fig. 2 also presents the mass properties of finned projectile.

The computational mesh for the projectile is illustrated in Fig. 3. Tab. 1 presents the initial conditions of the trajectory simulation. The equivalent free flight Mach number is 3. The Reynolds number is 7.083e7/*m*.

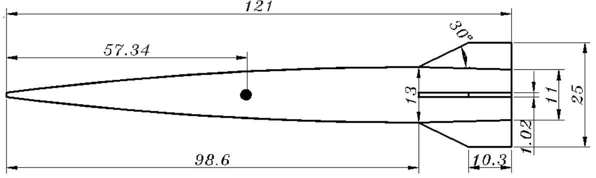

***Mass*=4.84e-2*kg*, *Ixx*=7.40e-7*kg.m*^{2},**
***Iyy* = *Izz*=4.84e-5*kg.m*^{2}**

Fig. 2. Geometric Parameter and Mass Properties of Spinning Projectile

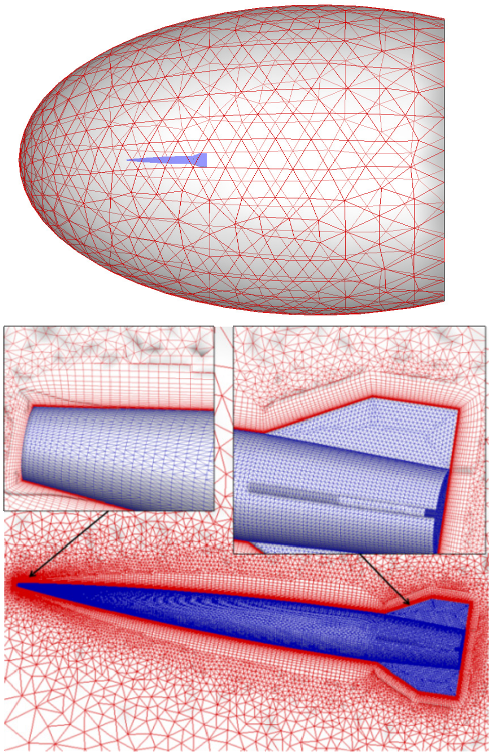

Fig. 3. Computational Mesh of Spinning Projectile

Tab. 1. Initial Conditions of Finned Projectile

Direction	Distance of C.G. (meter)	Speed of C.G. (m/s)	Euler angle (rad)	Angular velocity (rad/s)
X	4.593	1030.81	2.051	2518.39
Y	-0.200	22.064	0.088	-52.802
Z	-0.159	86.278	-0.023	22.233

Fig. 4 shows the variation of the attitude angle with distance traveled. The pitching angle is cyclical. Both the amplitude and the frequency agree well with the experimental data. The amplitude decreases with the distance traveled. The yaw angle also changes periodically. The amplitude decreases in the beginning and then goes into stable oscillation. The period agrees well with the experimental data.

Fig. 5 shows the computed *y* and *z* distances as a function of the range. The change trend is basically the same. Compares to the lateral displacement in y direction, the result in z direction is more close to the experimental data. Moreover, the oscillation in z direction is stronger than in y direction. The reason is that the change of pitching angle is greater than yaw angle in the flight process of the spinning projectile. It leads to the aerodynamic force in z direction changing more dramatically than in y direction. In addition, the orientation angles decrease due to the effect of air resistance, the change of the aerodynamic forces/moments also decrease. The y and z displacement curves reflect the attenuate trend of oscillation.

Fig.6 shows the comparison of the predicted aerodynamic forces in three directions with the data extracted from Ref. 18. Curve in the figure is the result of numerical calculation in this paper. The x direction aerodynamic force agrees well with the data in Ref. 10 when x<30m. When x>30m, amplitude and period gradually declined and the calculation value is a little smaller than the results in Ref. 18. Y and Z direction aerodynamic forces fit well with Ref. 18 in the simulation process. Comparing the Y and Z direction aerodynamic force curves with the yaw and pitching curves, they are very similar. It means that the aerodynamic forces change with the orientation angles. The pitching moment in inertial coordinate system is also shown in Fig.6. The Y direction aerodynamic moment curves agree well with the results of Ref. 18 during the simulation process and it is similar with the corresponding orientation angle curves.

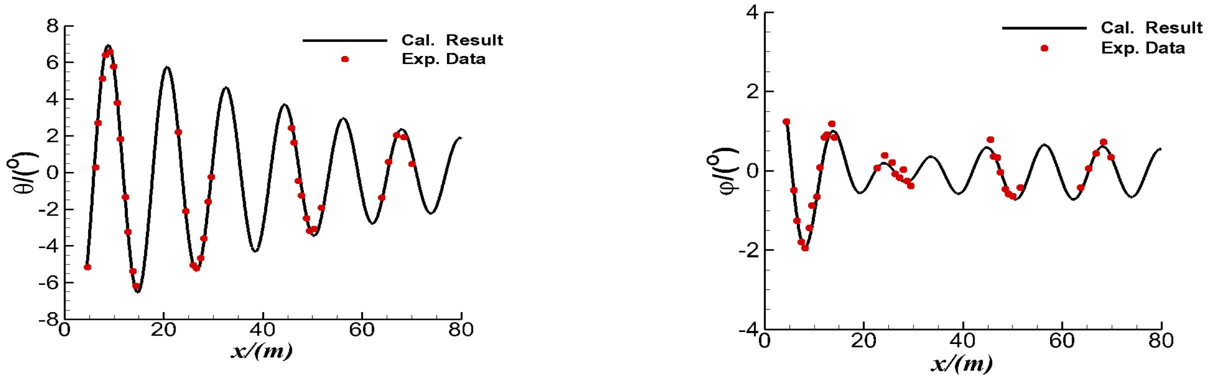

Fig. 4. Attitude Angle vs. Range

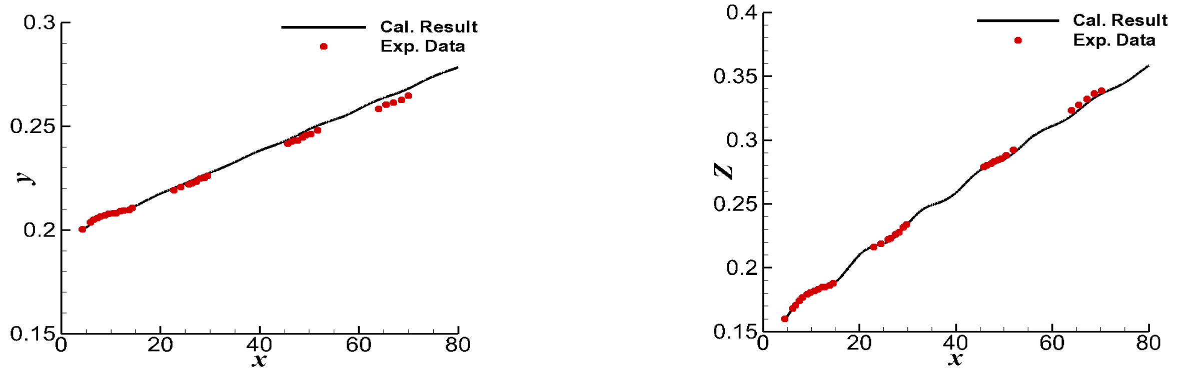

Fig. 5. Trajectory Simulation vs. Range

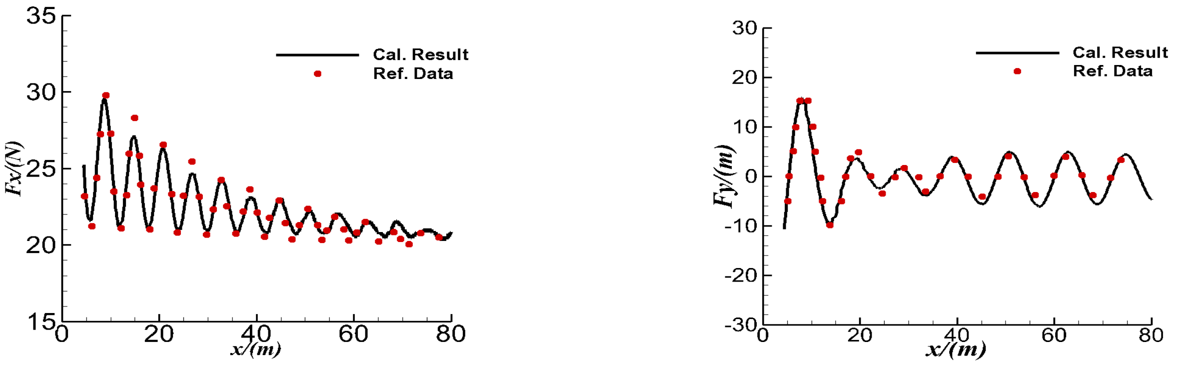

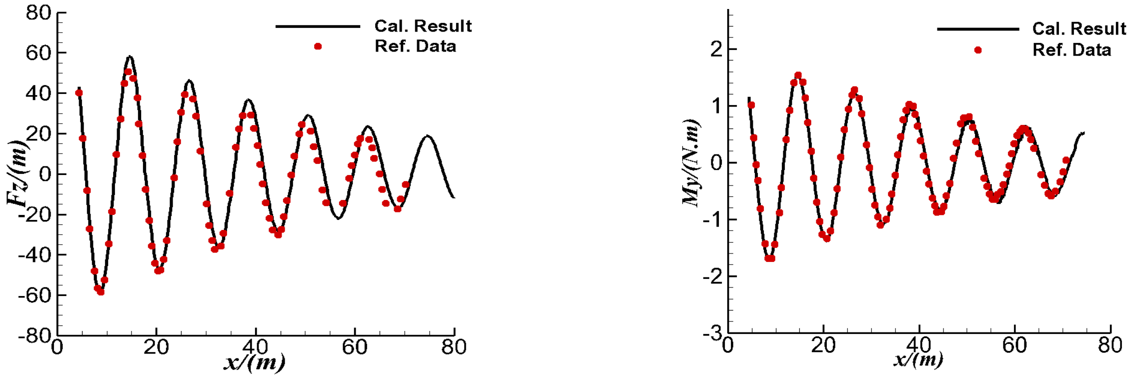

Fig. 6. Aerodynamic Forces/Moments vs. Range

3.2 Verification Case of Static Aeroelsticity

The aeroelastic study of the HIRENASD wing-body [19] is selected to evaluate the accuracy of static aeroelsticitic simulation of the solver presented in this paper. The configuration and the hybrid meshes (illustrated in Fig. 7) are provided by the AePW Conference sponsors. This simulation is performed at a Mach number of 0.80, a Reynolds number of 14 million and a q/E ratio of $0.47 \times 10e\text{-}6$, (q is the dynamic pressure of the free stream, and E is the elastic modulus of the structure), since interesting transonic flow phenomena and significant wing deformations were found in the experiment [19]. Fully turbulent solution is adopted for viscous flow by using SA model and an IDW method is applied for mesh deformation.

Fig. 8 plots the comparison between the measured data and the calculated bending deformations of the leading edge and the trailing edge at the wing tip at an angle of attack equal to 3 degree. There are significant deformations occurred and the calculated deformations have good agreement with experimental data, which gives a reliable impression of the quality of the numerical simulation concerning the flow field and the interaction with the elastic structure.

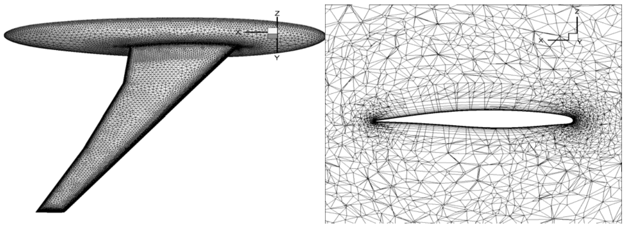

Fig. 7. Boundary Mesh and Clip of HIRENASD Model

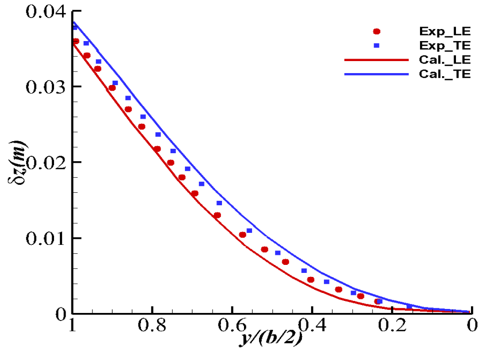

Fig. 8. Comparison of the Deformation between Calculated and Experimental Results

3.3 Free flight Case of flexible Projectile

In order to improve the speed and the range of practical projectiles, engineers tend to increase the ratio of slenderness and decrease the structural weights for more fuel. However, it is easier for these structures to deform due to their low rigidity. Accordingly, the trajectory of aerial separation cannot be predicted accurately regardless of elastic effect. Here, a projectile model similar to AIM-7 is constructed to study the influence of aeroelasticity on the characteristic of flight dynamics.

3.3.1 Computational Model

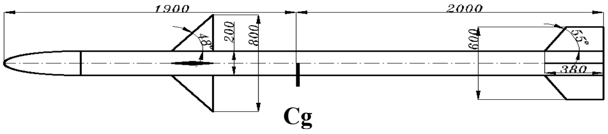

***Mass*=291.6*kg*, *Ixx*=25.6*kg.m*^{2}, *Iyy* = *Izz*=351*kg.m*^{2}**

Fig. 9. Geometric Model and Parameter of the Projectile with Large Slenderness Ratio

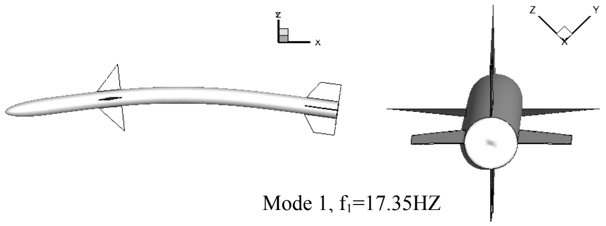

Mode 1, f_1=17.35HZ

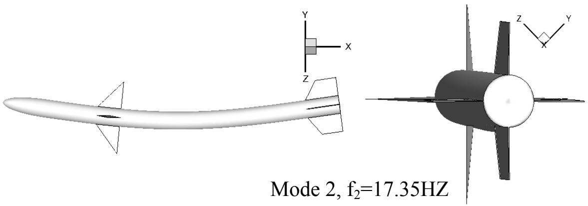

Mode 2, f_2=17.35HZ

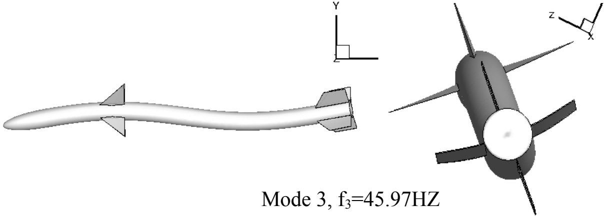

Mode 3, f_3=45.97HZ

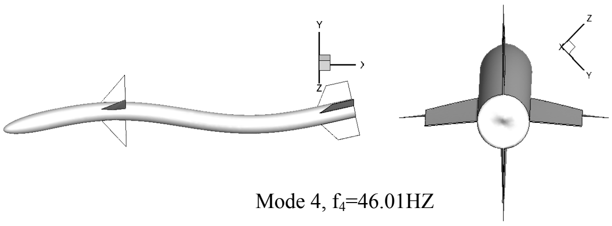

Mode 4, f_4=46.01HZ

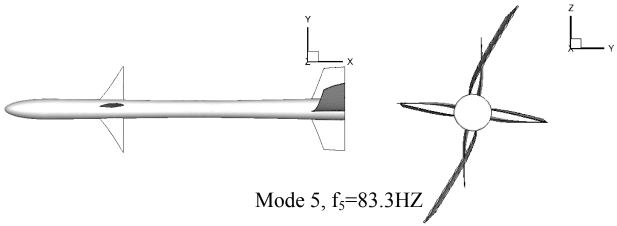

Mode 5, f_5=83.3HZ

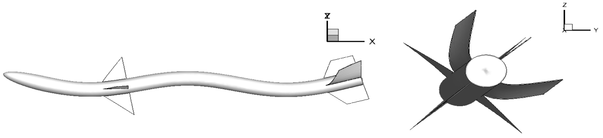

Mode 6, f_6=87.7HZ

Fig. 10.First Six Modes and Natural Frequencies

The computational geometry and corresponding parameters are illustrated in Fig.9 Here, according to the mass distribution of the structure, the inertial properties of the projectile are computed with the modeling software Patran. Since the displacement due to elastic deformations is much smaller than the characteristic scale of the projectile, the centroid position and inertia moments are assumed to be constant during the flight process. It is necessary to get generalized mass, free frequencies, modes and other dynamic parameters when using the mode-summation method. MSC.Nastran is adopted here to undertake modal analysis and obtain the modes of the first sixteen orders including the main dynamic character of the body, the wings and the control surfaces respectively. Fig. 10 presents the first six modes.

3.3.2 Results and Analysis

The orientation angles and angle velocities around the centroid of both rigid models and elastic ones are depicted in Fig. 14 and Fig. 15 respectively. Although there is some significant difference between the two types of models, the final steady state of orientation angles and angle velocities are almost the same. And the oscillation of the pitch angle attenuates at the end since the centroid is in front of the aerodynamic center. However, the oscillatory cycles increase when deformations appear, which is in accordance with conclusions of Ref [20]. The reason of this phenomenon is that the aerodynamic center moves forward because of deformations, resulting in the decrease of static stability margin.

Responses of aerodynamic forces and aerodynamic moments are illustrated in Fig. 13 and Fig.16 respectively. Aerodynamics oscillatory cycle of the elastic model are longer than that of the rigid model, which is similar to results of the displacements shown in Fig. 11 and the orientation angles shown in Fig. 14. Although the response histories are different, the steady states of elastic and rigid models agree substantially.

Fig. 17 presents generalized displacements of the first six structural modes. It is obvious that the first two bending modes of the body play a dominant role in deformations. The influence of third and fourth order modes is not as great as the first two, but it cannot be ignored. The amplitudes of the generalized displacements behave oscillating at the beginning, while they converge to the steady states.

In order to understand the mechanism of the effect of the elastic deformation on the trajectory of flexible projectiles, the trajectory of another rigid model with the centriod moved backward is investigated. The location of centroid in Fig. 9 is 2.00 meters away from the nose of the body. Computational results of the pitch and yaw angle shown in Fig. 18 indicate that the response history of the rigid model with centroid moved backward (marked with "_rigid_bw") is more close to the result of the flexible model with the original centroid location, though some distinction exists in the amplitudes. Comparison results could provide the explanation of the effect of aeroelasticity that the elastic deformation moves the aerodynamic center forward. From Ref [21], the angular rate of the oscillation in the longitudinal direction could be expressed in Eq. (15)

$$\omega_{Lg}^2=\frac{1}{I_y}q_\infty S_W C_{AW} C_{L\alpha}\left[(x_{ac}-x_{cg})-C_{mq}/2\mu\right] \quad (15)$$

Where ω_{Lg} is the angular rate of longitudinal oscillation. q_∞ is the dynamic pressure of the free stream. S_W and C_{AW} are the wing area and the aerodynamic chord of the wing respectively. $C_{L\alpha}$ is the slope of the lift coefficient relative to the angle of attack. x_{ac} and x_{cg} are the aerodynamic center and the centroid location. C_{mq} is the slope of the longitudinal moment relative to the pitch rate, and μ is the dimensionless density. For the projectile model researched in this paper, q_∞, S_W, C_{AW} and μ are unrelated to the rigidity of the models, while $C_{L\alpha}$ and C_{mq} are less sensitive to the deformation. Thus, the stability margin is mainly determined by the distance between the aerodynamic center and the centroid location. Since the centroid of the original rigid model is in front of the aerodynamic center, i.e. and the configuration is stable ($x_{ac}-x_{cg}$>0), the elastic deformation decreases the distance between the centroid and the aerodynamic center, which could decrease ω_{Lg} and correspondingly increase the oscillation cycle. Furthermore, it can be inferred that the aerodynamic center of the flexible model might be moved in front of the centroid, which would make the aerodynamic configuration unstable, if the stability margin is much smaller or the structural stiffness is rather lower.

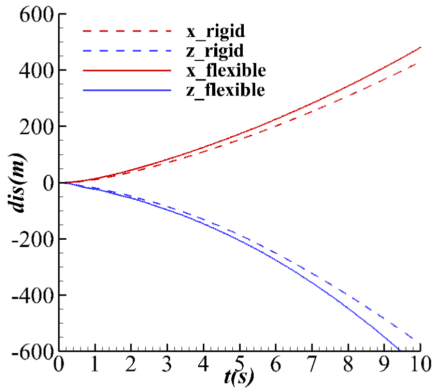

Fig. 11. History of the Location of the Centroid

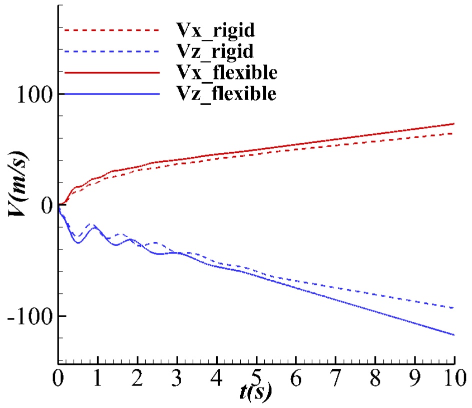

Fig. 12.History of Centroid Velocities

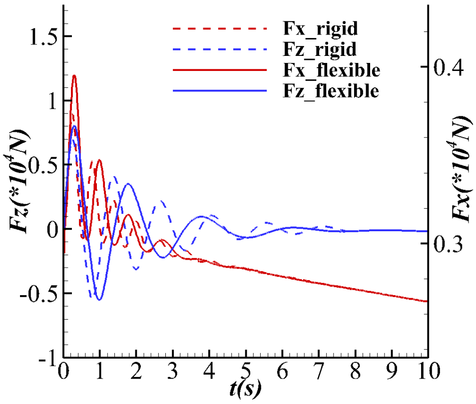

Fig. 13. History of Aerodynamic Forces

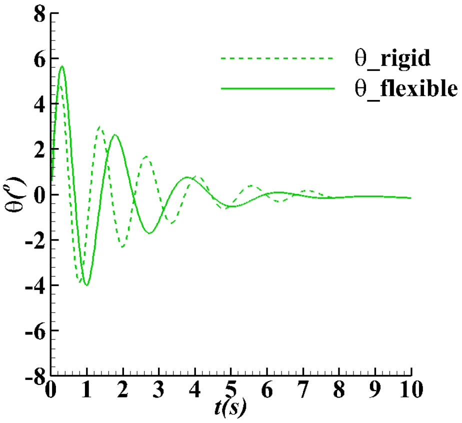

Fig. 14. History of Orientation Angles

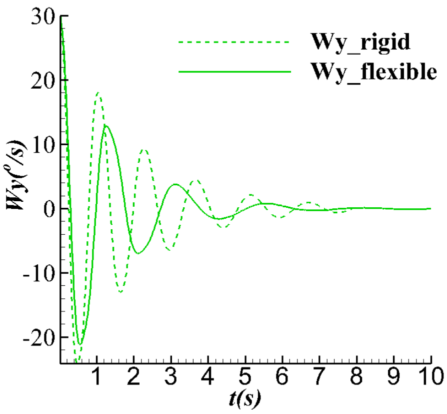

Fig. 15. History of Angular Velocities

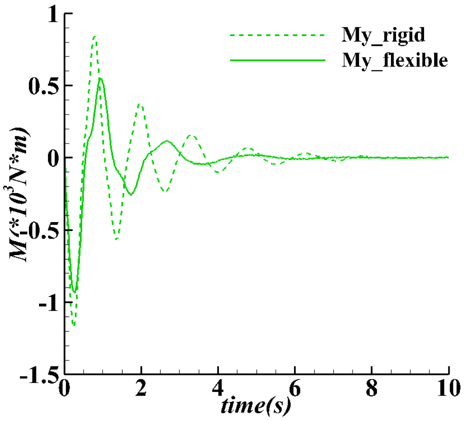

Fig. 16. History of Aerodynamic Moments

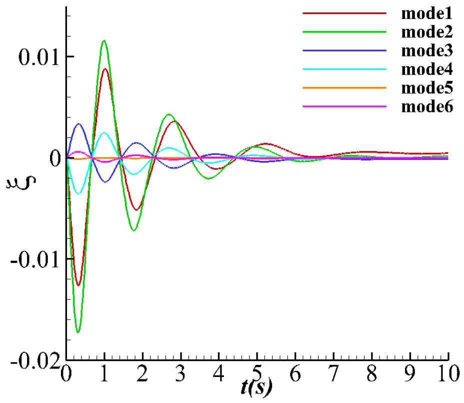

Fig. 17. General Displacement of Flexible Model

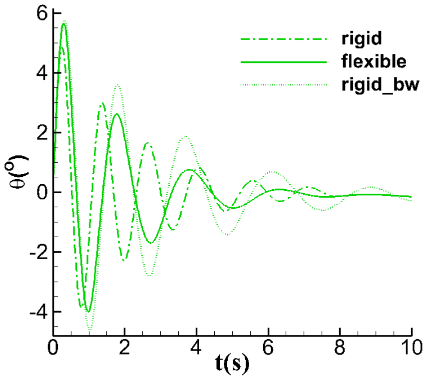

Fig. 18. History of Orientation Angles of Various Model

References

[1] Cochran J. E., Christensen D. E.. Free-Flight rocket attitude motion due to transverse vibration. J Spacecr Rockets, Vol. 17, No. 5, pp 425-431,1980

[2] Beal T R. Dynamic stability of flexible missile under constant and pulsatng thrusts. AIAA J, Vol. 3, No. 3, pp 486-494,1965

[3] Meirovitch L., Wesley D. A.. On the dynamic characteristics of a variable-mass slender, elastic body under high accelerations. AIAA J, Vol. 5, No. 8, pp 1439-1447,1967

[4] Zang T. C., Hu H. X.. A review of great slenderness ratio projectile elastic effect research. J Ballist, Vol. 11, No. 3, pp 89-93, 1999

[5] D. H. Latus. Aeroeleastic stability of slender, spinning missile. J Guid Control Dyn, Vol.15, No.1,pp 144-191,1992

[6] Reis,G. E. Sundery W. D.. Calculated aeroelastic bending of a sounding rocket based on flight data. J Spacecr Rockets, Vol. 4, No.11, pp 1489-1494,1967

[7] Womack W. C., Bert C. W.. Perdreauville F. J.. Dynamics of Sounding Rockets at Burnout. J Spacecr Rockets, Vol. 11, No. 10, pp 716-720, 1973

[8] Wang L. M.. An analysis on the flexibility in flight of projectiles or rockets having high L/D ratios. Acta rmamentarii, Vol. 21, No. 2, pp 108-111 , 2000

[9] Schütte A., Einarsson G., Raichle A.. Numerical simulation of maneuvering aircraft by aerodynamic, flight-mechanics, and structural-mechanics Coupling. J Aircraft, Vol 46, No. 1, pp 53-64,2009

[10] Meakin R. L., Atwood C. A., Hariharan N.. Development, deployment and support of a set of multidisciplinary, physics-based simulation software products. In: 49th AIAA Aerospace Sciences Meeting including the New Horizons Forum and Aerospace Exposition, Orlando. AIAA Paper 2011-1104, 2011

[11] Morton S. A., McDaniel D. R., Sears D. R.. Kestrel v2.0-6DOF and control surface additions to a CREATE simulation tool. In: 48th AIAA Aerospace Sciences Meeting Including the New Horizons Forum and Aerospace Exposition, Orlando. AIAA Paper 2011-1104

[12] Luke E., Collins E., Blades E.. A fast mesh deformation method using explicit interpolation. J Comput Phys, Vol. 231, No. 2, pp 586-601,2012

[13] G. Wang. New type of grid generation technique together with the high efficiency and high accuracy scheme researches for complex flow simulation. Xi'an: Northwestern Polytechnical University, 2005.

[14] Zhang W.W., Jiang Y.W., Ye Zhengyin. Two better loosely coupled solution algorithms of CFD based aeroelastic simulation. Engineering Applications of Computational Fluid Mechanics, Vol.1, No. 4, pp 253-262, 2007.

[15] Neumann J., Ritter M.. Steady and unsteady aeroelastic simulations of the hirenasd and wind tunnel experiment. IFASD 2009-132, 2009.

[16] Thomson W. T., Dahleh M.D.. Theory of vibration with application. New Jersy: Prentice-Hall Inc, 1998.

[17] Davis B. S., Guidos, B. J., Harkins T. E., Complementary Roles of Spark Range and Onboard Free-Flight Measurements for Projectile Development, US Army Research Lab, Aberdeen Proving Ground, MD, Weapons and Materials Research Directorate, 2009.

[18] Sahu J., Time-accurate Numerical Prediction of Free-flight Aerodynamics of a Finned Projectile, J Spacecr Rockets, Vol.45, No.5, pp 946-954, 2008

[19] https://c3.nasa.gov/dashlink/static/media/other/HIRENASD_base.htm

[20] HUA R.H. ZHAO C.X., YE Z.Y., etc. Effect of elastic deformation on the trajectory of aerial separation, Aerosp Sci Technol, Vol. 45, No. 9, pp 128-139, 2015

[21] Fang Z. P.. Flight dynamics of airplane. Beijing: Beijing University of Aeronautics and Astronautics Press, 2005.

Copyright Issues

Contact Author Email Address

HUA Ruhao: huaruhao@mail.nwpu.edu.cn
YE Zhengyin: yeyz@nwpu.edu.cn
YANG Lei: yangyichuan0768@163.com